Tailoring the topological surface state in ultrathin α-Sn(111) films

V. A. Rogalev [⊙],[1] F. Reis,[1] F. Adler,[1] M. Bauernfeind,[1] J. Erhardt,[1] A. Kowalewski,[1] M. R. Scholz,[1] L. Dudy,[1] L. B. Duffy,[2]
T. Hesjedal [⊙],[2] M. Hoesch,[3,4] G. Bihlmayer,[5] J. Schäfer,[1] and R. Claessen [⊙][1]

[1]*Physikalisches Institut and Würzburg-Dresden Cluster of Excellence ct.qmat, Universität Würzburg, 97074 Würzburg, Germany*
[2]*Clarendon Laboratory, Physics Department, Oxford University, OX1 3PU Oxford, England, United Kingdom*
[3]*Diamond Light Source, OX11 0DE Didcot, England, United Kingdom*
[4]*DESY Photon Science, Notkestraße 85, D-22607 Hamburg, Germany*
[5]*Peter Grünberg Institut, Forschungszentrum Jülich and JARA, 52425 Jülich, Germany*

We report on the electronic structure of α-Sn films in the very low thickness regime grown on InSb(111)A. High-resolution low photon energy angle-resolved photoemission spectroscopy allows for the direct observation of the linearly dispersing two-dimensional (2D) topological surface state (TSS) that exists between the second valence band and the conduction band. The Dirac point of this TSS was found to be 200 meV below the Fermi level in 10-nm-thick films, which enables the observation of the hybridization gap opening at the Dirac point of the TSS for thinner films. The crossover to a quasi-2D electronic structure is accompanied by a full gap opening at the Brillouin-zone center, in agreement with our density functional theory calculations. We further identify the thickness regime of α-Sn films where the hybridization gap in the TSS coexists with the topologically nontrivial electronic structure and one can expect the presence of a one-dimensional helical edge state.

I. INTRODUCTION

The low-temperature α phase of Sn belongs to a family of materials with a topologically nontrivial electronic band structure [1]. Due to its monoelemental nature, and the resulting favorable defect chemistry, α-Sn has recently attracted considerable interest [2–9]. In particular, α-Sn thin films grown by molecular-beam epitaxy (MBE) exhibit outstanding quality [5,8,10]. In contrast to Bi_2X_3 compounds ($X =$ Se or Te), band inversion in bulk α-Sn involves the *second* valence band (VB) Γ_7^- and conduction band (CB) Γ_8^+, which reveal *s*-like and *p*-like character, respectively [11]. Such band order is also typical of HgTe [12,13] and some half-Heusler compounds [14] and results in fact in a double band inversion with a pair of topological surface states (TSSs) of different wave-function localization character [6]. Most of the substrates available for epitaxial growth provide an in-plane compressive strain for α-Sn films, which drives them into a Dirac semimetal phase [6,15] with both TSSs being fully degenerate with bulk states. Yet, previous studies on in-plane compressively strained α-Sn thin films revealed that the hybridization between the upper TSS, the focus of the present paper, and the bulk states is weak due to differences in the orbital composition [6,16]. This allows for the observation of a sharp $E(\vec{k})$ dispersion of this TSS in spin- and angle-resolved photoemission.

The (111) surface of α-Sn is of particular interest due to its close relationship to the family of two-dimensional (2D) honeycomb lattices in group-IV and -V high-*Z* materials, e.g., stanene [17] or bismuthene [18]. These have been widely investigated, both theoretically and experimentally, as a new platform for utilizing helical spin-polarized topological edge states [19]. Despite numerous reports on the fabrication of stanene on a variety of substrates [20–26], the experimental

studies of the three-dimensional (3D) to 2D crossover of the TSS in α-Sn films have remained scarce. With the reduced thickness, the 3D bulk band structure changes, developing a gaps due to increasing confinement in a quantum well (QW), and the surface-TSS and interface-TSS (at the α-Sn–substrate interface) wave functions start to overlap. Similar to HgTe/CdTe quantum wells [27,28], the band inversion in α-Sn can be lost at certain critical thickness [3,29–31] or even show an oscillatory behavior [32] depending on thickness. Additionally, if the band inversion remains, the hybridization between the surface TSS and interface TSS in thin α-Sn films could open a gap at the Dirac point (DP). At the same time a strong confinement of the 2D TSS on the side planes leads to the appearance of the one-dimensional (1D) helical edge states. In such case the system often can be classified as a 2D quantum spin Hall insulator (QSHI).

In this paper we report on the electronic structure of ultrathin α-Sn films epitaxially grown on InSb(111)A and, in particular, on the evolution of the TSS as a function of thickness exploiting high-resolution angle-resolved photoemission spectroscopy (ARPES) and density functional theory (DFT) calculations which notably include the substrate. We find that, in contrast to α-Sn on InSb(001), the DP of the TSS for the (111) surface orientation is situated significantly below the Fermi energy for 10-nm-thick α-Sn films. The latter enables the direct observation of the hybridization gap opening at the DP for thinner films. Thus, for a 3-nm-thick film we find a gap in the TSS of the order of $\Delta E_{peak}^g \approx 200$ meV (peak to peak). The electronic structure of the quasi-2D 1-nm-thick films exhibits a full gap opening at the Γ point ($\Delta E_{peak}^g \gtrsim 400$ meV). Our DFT calculations for thin α-Sn films on InSb(111)A show good agreement with the experimental data and provide evidence for the spin-polarized character of

the TSS. Furthermore, we establish that coexistence of the TSS hybridization gap and the topologically nontrivial band structure appears in a narrow α-Sn film thickness range of $\approx$2–10 nm, at which one can expect also the presence of a 1D helical edge state. In addition, we report on an 8×8 surface reconstruction observed in low-energy electron diffraction (LEED) and scanning tunneling microscopy (STM).

II. METHODS

α-Sn thin films were grown by MBE on *n*-doped In-terminated InSb(111) substrates. The eight-effusion cell MBE system is directly attached to the high-resolution ARPES system at beamline I05 at the Diamond Light Source (Didcot, UK), allowing for in-vacuum transfers [33]. The substrates were cleaned by several cycles of Ar ions sputtering and annealing until a clear 2×2 reconstruction was observed by LEED [see Fig. 1(a)]. During thin-film growth, the InSb(111) substrates were held at ambient temperature and the α-Sn film quality was monitored by reflection high-energy electron diffraction (RHEED). The thickness of the Sn layers was varied by changing the deposition time while keeping the flux from the effusion cell constant. As in the case of (001)-oriented films [16], the x-ray photoemission spectroscopy (XPS) data indicate the presence of In atoms on the (sub)surface of α-Sn films, which could be a result of In interdiffusion and/or In surface segregation that appears during substrate cleaning.

ARPES measurements have been carried out primarily with *p* linearly polarized light unless stated otherwise, at varying photon energies at beamline I05. ARPES data measured with *s*-polarized light are shown in the Supplemental Material [34]. The endstation is equipped with a Scienta R4000 hemispherical electron analyzer that provides an ultimate energy and angular resolution of $\approx$5 meV and $0.1°$, respectively.

STM experiments were performed with an Omicron low temperature (LT)-STM at a base pressure $p < 5 \times 10^{-11}$ mbar ($T = 4$ K) using tungsten tips tested on a Ag(111) single crystal for sharpness and spectroscopic properties.

For the DFT calculations we used the full-potential linearized augmented plane-wave method [35] as implemented in the FLEUR code in the thin-film geometry [36]. In this way electrostatic interactions that occur for polar films in repeated-slab calculations are avoided. The muffin-tin radii for Sn, Sb, and In were chosen to be 2.3 a.u., while for H we used 0.9 a.u. The $4d$ orbitals of Sn and Sb were included as local orbitals. The plane-wave cutoff was 3.8 a.u.$^{-1}$ for the wave functions and 16.3 a.u.$^{-1}$ for the potential. We used a 9×9 Monkhorst-Pack *k*-point grid to sample the Brillouin zone and employed the local density. We employed the local density approximation to the exchange-correlation potential [37]. Our models for the 0.7- and 2.5-nm Sn films included four InSb(111)A substrate layers that were charge compensated on both sides by ± 0.25 electronic charges in the virtual crystal approximation to simulate a flat profile of the band edges. The potential profile was checked by monitoring the layer dependence of the $2s$ core levels. The 7.1-nm film was calculated without substrate and in all cases hydrogen was deposited on the upper and lower surface of the film to saturate dangling bonds. By relaxation we obtained Sn-H
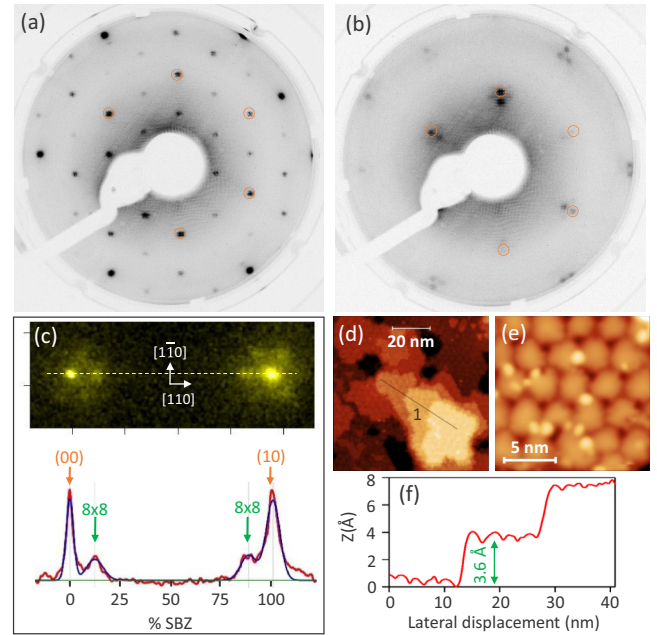

FIG. 1. (a) LEED taken at $E = 45$ eV on a clean InSb(111)A substrate exhibits 2×2 surface reconstruction [orange circles denote 1×1 spots]. (b) LEED taken at $E = 45$ eV on 10 nm-thick α-Sn(111) film. Apart from the expected 1×1 structure (orange circles), additional spots of high-order surface reconstruction are observed. (c) Spot-profile analysis LEED data taken at $E = 87$ eV and corresponding line profile (data plotted in red, four-peaks fit plotted in blue) through (00) and (10) spots allow us to assign the new surface reconstruction to be 8×8. (d) STM data measured with $U = 2$ V, $I = 50$ pA at $T = 4$ K. (e) STM data on a smaller scale showing domains. (f) The height profile along the path labeled "1" in (d) reveals a step height of 3.6 Å.

and Sb-H distances of 1.71 and 1.75 Å, respectively, which is a bit longer than in SnH$_4$ (1.69 Å) and SbH$_3$ (1.70 Å). Although in the experiment other atomic species might saturate the dangling bonds at the surface, with H termination we simulate successfully the observed absence of the dangling-bond states at the Fermi level. To achieve a correct band ordering we applied the DFT+U scheme as described in Ref. [2]. The same correction was applied to InSb, where the band gap is also underestimated in DFT. The films were relaxed and spin-orbit coupling was applied in a self-consistent manner [38].

III. EXPERIMENTAL RESULTS

During growth, RHEED reveals a well-resolved streak pattern consistent with the substrate symmetry, thus confirming the epitaxial growth of α-Sn films on InSb(111)A substrate. However, in LEED, apart from the main 1×1 pattern, as-grown α-Sn films show additional spots stemming from a surface reconstruction: Instead of the commonly observed 3×3 surface reconstruction, we find a higher-order spots [Fig. 1(b)]. Spot-profile analysis LEED allowed us to identify an 8×8 surface reconstruction [Fig. 1(c)]. It persists when mildly annealing the sample at $T \approx 150\,°$C, leading to sharper LEED and ARPES signals. When the annealing temperature
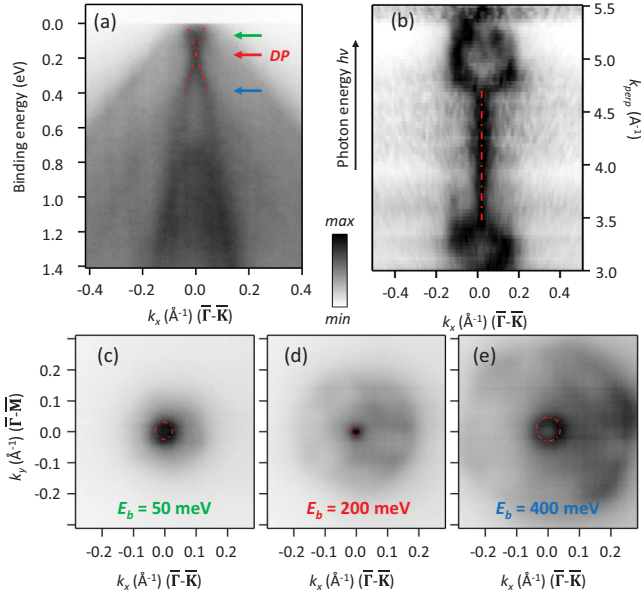
FIG. 2. Experimental electronic structure of a 10-nm-thick α-Sn film on InSb(111)A. (a) Band map measured at a photon energy of $h\nu = 18$ eV and at $T = 8$ K along the $\overline{\Gamma}$-$\overline{K}$ direction. (b) Photon energy scan between $h\nu = 33$ and 120 eV ($\mathbf{k}_\perp \approx 3$–5.5 Å^{-1}), taken with the entrance slit oriented along the $\overline{\Gamma}$-$\overline{K}$ direction ($E_B = 100$ meV). The spectra have been normalized to have equal intensity for each $\mathbf{k}_\perp$. (c–e) Stacks of experimental constant energy contours at different E_B. Red dotted lines are guides for the eye indicating the TSS.

FIG. 3. ARPES band maps as a function of α-Sn film thickness. The photon energy was 18 eV and the temperature was 8 K. EDCs at normal emission are overlayed on the left of each panel. (a) 10-, (b) 3-, and (c) 1-nm-thick α-Sn films. (d) Clean InSb(111)A substrate.

is increased further, the LEED pattern changes to the 1 × 1 reconstruction, in agreement with other studies [39,40]. In addition, we performed STM measurements of 10-nm-thick α-Sn films, which are summarized in Figs. 1(d)–1(f). The STM measurements reveal domains with a shape close to hexagonal, which could result from twinning, i.e., an overlap of two 60°-rotated triangular domains. Twinning was indeed reported for α-Sn films on Hg$_{0.8}$Cd$_{0.2}$Te(111) substrates [41]. The lateral size of domains ranges from a factor-7 to a factor-8 lattice constant of unstrained α-Sn ($a = 4.59$ Å). The step height $h \approx 3.6$ Å is consistent with the interplanar distance between bilayers of α-Sn(111) films of 3.75 Å. Additional STM or scanning tunneling spectroscopy measurements are necessary to establish the exact structural model of this reconstruction.

Figure 2(a) shows ARPES data obtained on a 10-nm-thick α-Sn film using a photon energy of $h\nu = 18$ eV. Such photon energy corresponds to a surface perpendicular momentum $\mathbf{k}_\perp = 1.33 \times (2\pi/c)$, assuming an inner potential of $V_0 = 5.8$ eV [6] and $c = 3.75$ Å (interplanar distance between bilayers in α-Sn), which allows us to highlight the surface states [6,16]. The very presence of a well-ordered surface provides good quality ARPES data, while any signature of the 8 × 8 reconstruction in the electronic structure is not observed. The Fermi level is pinned ≈ 100 meV below the valence-band maximum of the projected bulk bands [Fig. 2(a)], therefore the expected band gap in the bulk electronic structure defined by quantum confinement [30] is not accessible. Apart from the projected bulk bands that possess 60°-twinned threefold
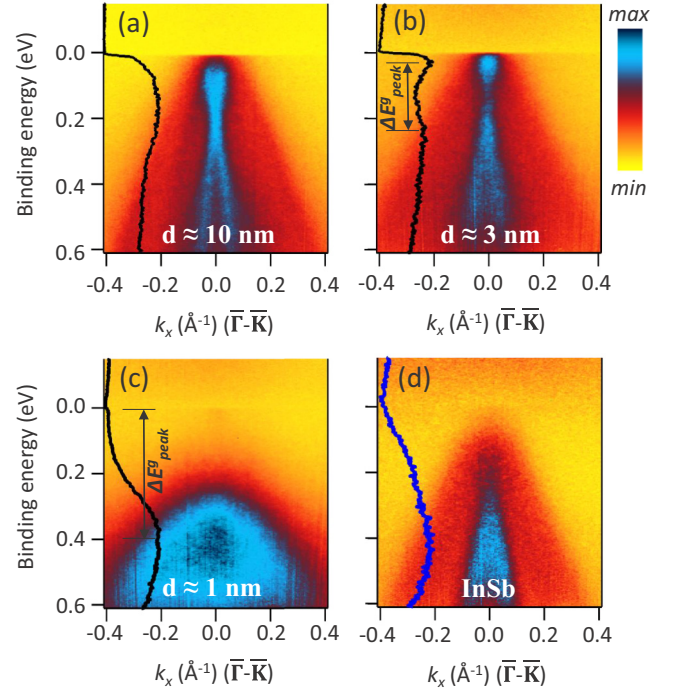
character visible in Figs. 2(c)–2(e), the electronic structure of α-Sn films harbors an additional pair of linearlike crossing bands with a cross point ≈ 200 meV below E_F [Fig. 2(a)]. The linearlike band has a group velocity $v_{TSS} = (6.4 \pm 0.5)$ eV Å, i.e., $(9.7 \pm 0.8) \times 10^5$ m/s [see Fig. 3(a)], which is slightly bigger than the previously reported value for α-Sn [3,4,16]. However, in contrast to α-Sn on InSb(001) and InSb(111)B [15,22], our data reveal a TSS with a DP located higher in binding energy, which allows us to observe the TSS branches below and above the DP. We note that due to the doping level of our α-Sn films, as well as the limited ARPES resolution, we are not able to observe (gapped) topological surface states in the meV range near the CB minimum which were recently reported in transport data of HgTe films [42].

The two-dimensional character of the TSS is experimentally further confirmed by measuring ARPES at different photon energies [Fig. 2(b)]. Clearly, the TSS shows no dispersion with varying photon energy ($\mathbf{k}_\perp$ momentum). At the photon energies corresponding to the bulk Γ points in the surface normal direction the intensity of the bulk bands starts to dominate {$\mathbf{k}_\perp = 3.3$ Å^{-1}[2×(2π/c)] and 5.0 Å^{-1}[3×(2π/c)]}. We note that, similar to the case of the (001) surface, the momentum distribution of the TSS at given binding energies is isotropic in the $\mathbf{k}_\parallel$ plane and does not show any noticeable warping effects [Figs. 2(c)–2(e)].

The clear visibility of the DP allows for probing the possible opening of a hybridization gap in the TSS upon reducing the α-Sn film thickness, i.e., to observe a transition from a quasi-3D topological insulator (TI) to a quasi-2D TI with a
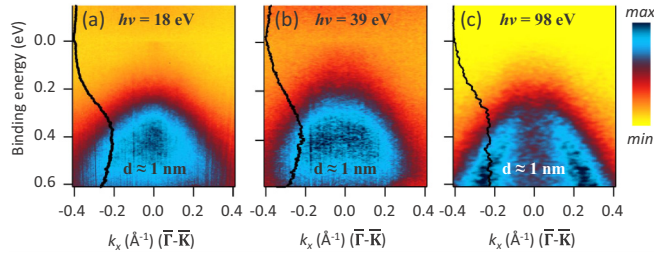
FIG. 4. ARPES data measured on a 1-nm-thick α-Sn film at different photon energies $h\nu$ of 18 eV (left), 39 eV (center), and 98 eV (right). EDCs at normal emission are overlayed in each panel.

gapped TSS. Figure 3 shows ARPES maps for different α-Sn film thicknesses. The energy distribution curves (EDCs) taken at $k_x = 0$ are overlayed on the left-hand side of each map. Despite the relatively thin film thickness of only 10 nm, the EDC taken through the DP does not reveal any hybridization gap in the TSS [Fig. 3(a)].

With the thickness reduced to 3 nm we observe a slight p-doping effect in the electronic structure (energy shift $\Delta E \approx 80$ meV). Such a behavior is consistent with the shift of the VB offset of ≈ 100 meV for thinner α-Sn films (determined by XPS, not shown here). The band gap in the projected bulk electronic structure remains unresolved in ARPES as it is still situated above the E_F. However, a clear reduction of the spectral weight at the DP is observed for the 3-nm-thick film [Fig. 3(b)]. This is likely a result of the TSS hybridization between the surface TSS and interface TSS. We can estimate the characteristic decay length of the 2D TSS as $l_{\text{decay}} = \hbar v_{\text{TSS}}/E_g = 1.3$ nm [43,44], where $E_g = 0.7$ eV is the gap between the inverted Γ_8^+ and Γ_7^- bands in bulk α-Sn [6]. The surface TSS and interface TSS start to significantly hybridize at α-Sn film thickness of $d_{\text{hybr.}} = 2 \times l_{\text{decay}} \approx 2.6$ nm, which is in good agreement with our data. However, instead of a well-defined hybridization gap, the corresponding EDC taken at the Γ point shows a rather broad local minimum at the DP, which could be a combined effect of the background of the projected bulk states and lateral fluctuations in energy positions of the surface TSS and interface TSS. The energy difference between the EDC maxima is found to be $\Delta E_{\text{peak}}^g \approx 200$ meV, which is again lower than the theoretical value for a CdTe/α-Sn quantum well [30]. This discrepancy is most probably due to the more relaxed boundary conditions. Interestingly, gapping of the TSS was not resolved in α-Sn(001) thin films of similar thickness (3–4 nm) grown on a InSb(001) substrate, yet for the thicker films (≈ 5 nm) a TSS gap of ≈ 200 meV was reported [3]. The latter was attributed to hybridization of the TSS with bulk QW states.

Reducing the film thickness further, the TSS hybridization becomes stronger. The 1-nm-thick α-Sn film reveals a total gap of $\Delta E_{\text{peak}}^g \gtrsim 400$ meV [see Fig. 3(c)] since the CB minimum is at or higher than E_F. In addition, the bulk electronic structure loses dispersive behavior in $\mathbf{k}_\perp$ due to a strong confinement. This can be seen in Fig. 4 where the $\mathbf{k}_\parallel$ dispersion shows only a minor variation with photon energy. As a consequence, we are not able to distinguish experimentally between hybridized TSS states and quasi-2D bulk states. Note that the measured film data are clearly distinct from those of a
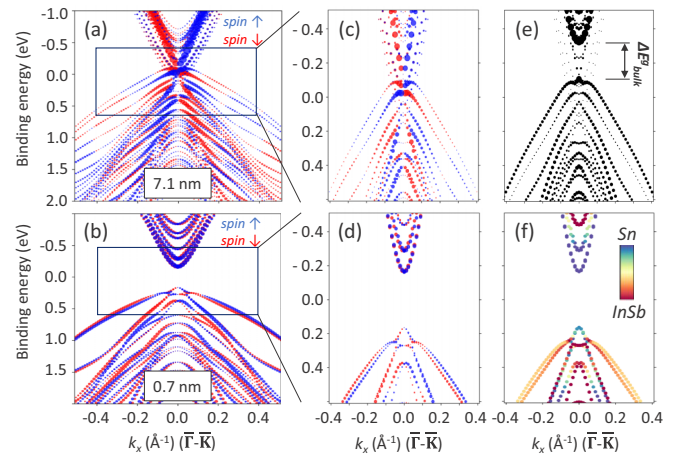

FIG. 5. DFT calculations of a 7.1-nm-thick (a), (c), (e) and 0.7-nm-thick (b), (d), (f) α-Sn film on InSb(111)A. (a)–(d) The blue and red colors denote the spin polarization, while the size of the circles is a measure of the *surface* density of states of the α-Sn film. (e) The size of the circles is proportional to the α-Sn density of states in the middle of the α-Sn film, i.e., *bulk* states. (f) Same as (d), however here the color indicates the respective contributions from the Sn and InSb states.

clean InSb substrate [Fig. 3(d)]. The quasi-2D character of the bulk electronic structure of the 1-nm-thick film is consistent with the data reported in Ref. [22] for bilayer stanene on InSb(111)B. Nevertheless, our results do not fully agree with the data reported in Refs. [15,22] for thicker α-Sn films since the quantum well and TSS hybridization effects are much more pronounced both in our calculations (see Fig. 5) and in the experimental data. We note that at such low α-Sn film thickness part of the photoelectrons from the substrate can reach the detector and contribute to the observed intensity in the ARPES maps. As a result one can notice a small nonzero photoemission intensity in the gap region near the Γ point in Figs. 4(b) and 4(c) [34].

In order to trace the change of the electronic structure with film thickness we performed DFT calculations. Figure 5 presents the calculation results obtained for 7.1-nm-thick (a), (c), (e) and 0.75-nm-thick (b), (d), (f) α-Sn films on InSb(111)A, respectively. The blue and red colors in Figs. 5(a)–5(d) denote the spin polarization, while the size of the circles is proportional to the density of states in the first two layers for the 0.75-nm-thick film, and above the layers for the 7.1-nm-thick films. Figures 5(c) and 5(d) show the enlarged region around E_F comparable to the experimental data presented in Fig. 3.

For the 7.1-nm-thick α-Sn film, the linearly dispersing spin-polarized surface states can be recognized in the electronic structure [Figs. 5(a) and 5(c)]. Yet, in contrast to the experimental data, the DP is located in the vicinity of E_F [Fig. 5(c)], which, in turn, is close to the valence-band maximum. Apart from this mismatch in the energy position that depends on the alignment of the potentials between the substrate and the α-Sn film, the theoretical data agree well with the experimental TSS shown in Fig. 2(a). The size of the dots in Fig. 5(e) is proportional to the density of states in the center of the α-Sn film, and thus reveals a quantum

TABLE I. Experimental TSS hybridization gap and theoretical s-like and p-like band order near E_F at the Γ point as a function of α-Sn thickness in the α-Sn/InSb(111)A system.

α-Sn thickness	TSS gap ΔE_{peak}^g	Band order
≈ 10 nm	Not resolved	Inverted
≈ 3 nm	≈ 200 meV	Inverted
≈ 1 nm	$\gtrsim 400$ meV	Trivial

confinement gap in the *bulk states* of $\Delta E_{bulk}^g \approx 200$ meV. The hybridization gap in the TSS [Fig. 5(c)] has a much smaller value of $\Delta E_{peak}^g \approx 30$ meV [34].

For the 0.7-nm-thick α-Sn film, a gap of ≈ 330 meV in the electronic structure is clearly resolved in the calculations [Figs. 5(b) and 5(d)], which agrees well with the experimentally determined gap of at least ≈ 400 meV [Fig. 3(c)]. We note that for such thin α-Sn films the calculated densities of states in the first two layers also contain a contribution from the InSb substrate states. However, as can be seen in Fig. 5(f), the calculated gap is mainly due to Sn states.

We further check the topological character of α-Sn thin films by tracking the relative energy positions of s-like and p-like bands near E_F as a function of thickness. The results are listed in Table I together with the values of the TSS hybridization gap estimated from the ARPES data. For the 7.1-nm-thick films the band order is inverted, i.e., a s-like minimum is below a p-like maximum. The band inversion remains also in 2.5-nm-thick films, where we find that the s-like band penetrates into the InSb substrate, thus enhancing the effective quantum well width. However, in the 0.7-nm-thick α-Sn film the s-like band position is now *above* the p-like band, which is a signature of a topologically *trivial* electronic structure. Therefore, the theoretical critical thickness for the transition to a trivial 2D insulator d_{crit} is between 0.7 and 2.5 nm and can be roughly estimated to have a value of $d_{crit} = 1.6$ nm. We note that the larger energy difference between s-like Γ_7^- and p-like Γ_8^+ bands in α-Sn, as compared to HgTe, leads to a different critical quantum well thickness below which the band inversion is lost. The electronlike band from the *gapped TSS* was calculated to cross the heavy-hole band near the Fermi level in CdTe/α-Sn(111) quantum wells at a critical thickness of 2.7 nm [30] (compare to $t_{crit} = 6.3$ nm for HgTe), defining the transition to a 2D trivial state. The topologically trivial band structure was also reported for 12-ML-thick (≈ 2 nm) α-Sn(001) films grown on InSb(001) substrate [3]. Moreover, the QSHI phase in freestanding α-Sn(001) films was calculated for thickness above $d_{crit} \approx 2$ nm [31]. In contrast to CdTe-based and freestanding (vacuum-based) quantum wells, the semiconducting InSb substrate allows for a less localized interface TSS at similar α-Sn film thickness, which, in turn, reduces the TSS hybridization and quantum well critical thickness.

Finally, we consider the quantum well confinement of the 2D TSSs that exist on the side planes parallel to the sample surface normal of the α-Sn film. From the uncertainty princi- ple we can approximately estimate the film thickness at which the uncertainty in the quasiparticle momentum is bigger than the typical 2D TSS momentum ($k_{typ.} = k_F \sim 0.02$ Å^{-1}, see Fig. 3) $d_{edge} \geqslant 1/k_{typ.} \approx 5$ nm, which defines the transition of the 2D TSS to the helical 1D edge states. Thus, for the α-Sn films with thickness between d_{crit} and ≈ 10 nm, one can expect the presence of a topologically protected 1D helical edge state, while the 2D TSSs remain gapped.

IV. CONCLUSIONS

In conclusion, we report on the electronic structure evolution of the TSS in MBE-grown α-Sn films on InSb(111)A as a function of film thickness. We observe an 8×8 surface reconstruction in 10-nm-thick films. As in the case of α-Sn on InSb(001), in 10-nm-thick α-Sn films the observed TSS is largely degenerate with the bulk band structure. However, the DP was found to be ≈ 200 meV below the E_F. This allows for the observation of a hybridization gap opening in the TSS for thinner α-Sn films: In 3-nm-thick α-Sn films we determine a gap in the TSS of the order of 200 meV. The crossover from the 3D to the quasi-2D stanenelike electronic structure in a 1-nm-thick film is accompanied by a full gap opening ($\Delta E_{peak}^g \gtrsim 400$ meV) at the Γ point in agreement with the calculated few-layer-stanene electronic band structure. Our DFT electronic structure calculations of thin α-Sn films on InSb(111)A show good agreement with the experimental data, as well as provide evidence for the spin-polarized character of the observed TSS. The latter, however, needs to be verified in future experiments. Furthermore, while we have identified the topologically nontrivial character of ≈ 10- and ≈ 3-nm-thick α-Sn films, we find no band inversion in the ≈ 1-nm-thick α-Sn film. Therefore, the thickness regime of α-Sn films where both the gapped TSS and topologically nontrivial band structure coexist is between ≈ 2 and ≈ 10 nm. In addition, this thickness regime corresponds to the appearance of topologically protected 1D helical edge states.

[1] L. Fu and C. L. Kane, Phys. Rev. B **76**, 045302 (2007).

[2] A. Barfuss, L. Dudy, M. R. Scholz, H. Roth, P. Höpfner, C. Blumenstein, G. Landolt, J. H. Dil, N. C. Plumb, M. Radovic, A. Bostwick, E. Rotenberg, A. Fleszar, G. Bihlmayer, D. Wortmann, G. Li, W. Hanke, R. Claessen, and J. Schäfer, Phys. Rev. Lett. **111**, 157205 (2013).

[3] Y. Ohtsubo, P. Le Fèvre, F. Bertran, and A. Taleb-Ibrahimi, Phys. Rev. Lett. **111**, 216401 (2013).

[4] S. Küfner, M. Fitzner, and F. Bechstedt, Phys. Rev. B **90**, 125312 (2014).

[5] J. C. Rojas-Sánchez, S. Oyarzun, Y. Fu, A. Marty, C. Vergnaud, S. Gambarelli, L. Vila, M. Jamet, Y. Ohtsubo, A. Taleb-Ibrahimi, P. Le Fèvre, F. Bertran, N. Reyren, J. M. George, and A. Fert, Phys. Rev. Lett. **116**, 096602 (2016).

[6] V. A. Rogalev, T. Rauch, M. R. Scholz, F. Reis, L. Dudy, A. Fleszar, M.-A. Husanu, V. N. Strocov, J. Henk, I. Mertig, J. Schäfer, and R. Claessen, Phys. Rev. B **95**, 161117(R) (2017).

[7] H. Huang and F. Liu, Phys. Rev. B **95**, 201101(R) (2017).

[8] Q. Barbedienne, J. Varignon, N. Reyren, A. Marty, C. Vergnaud, M. Jamet, C. Gomez-Carbonell, A. Lemaitre, P. Le Fèvre, F. Bertran, A. Taleb-Ibrahimi, H. Jaffrès, J.-M. George, and A. Fert, Phys. Rev. B **98**, 195445 (2018).

[9] M. Liao, Y. Zang, Z. Guan, H. Li, Y. Gong, K. Zhu, X.-P. Hu, D. Zhang, Y. Xu, Y.-Y. Wang *et al.*, Nat. Phys. **14**, 344 (2018).

[10] O. Vail, P. Taylor, P. Folkes, B. Nichols, B. Haidet, K. Mukherjee, and G. de Coster, Phys. Status Solidi B 1800513 (2019), doi: 10.1002/pssb.201800513.

[11] Z. Zhu, Y. Cheng, and U. Schwingenschlögl, Phys. Rev. B **85**, 235401 (2012).

[12] N. Berchenko and M. Pashkovski, Sov. Phys. Usp. **19**, 462 (1976).

[13] B. A. Volkov and O. A. Pankratov, JETP Lett. **42**, 178 (1985).

[14] S. Chadov, X. Qi, J. Kübler, G. H. Fecher, C. Felser, and S. C. Zhang, Nat. Mater. **9**, 541 (2010).

[15] C.-Z. Xu, Y.-H. Chan, Y. Chen, P. Chen, X. Wang, C. Dejoie, M.-H. Wong, J. A. Hlevyack, H. Ryu, H.-Y. Kee, N. Tamura, M.-Y. Chou, Z. Hussain, S.-K. Mo, and T.-C. Chiang, Phys. Rev. Lett. **118**, 146402 (2017).

[16] M. R. Scholz, V. A. Rogalev, L. Dudy, F. Reis, F. Adler, J. Aulbach, L. J. Collins-McIntyre, L. B. Duffy, H. F. Yang, Y. L. Chen, T. Hesjedal, Z. K. Liu, M. Hoesch, S. Muff, J. H. Dil, J. Schäfer, and R. Claessen, Phys. Rev. B **97**, 075101 (2018).

[17] A. Molle, J. Goldberger, M. Houssa, Y. Xu, S.-C. Zhang, and D. Akinwande, Nat. Mater. **16**, 163 (2017).

[18] F. Reis, G. Li, L. Dudy, M. Bauernfeind, S. Glass, W. Hanke, R. Thomale, J. Schäfer, and R. Claessen, Science **357**, 287 (2017).

[19] G. Li, Y.-Y. Zhang, H. Guo, L. Huang, H. Lu, X. Lin, Y.-L. Wang, S. Du, and H.-J. Gao, Chem. Soc. Rev. **47**, 6073 (2018).

[20] F.-F. Zhu, W.-J. Chen, Y. Xu, C.-L. Gao, D.-D. Guan, C.-H. Liu, D. Qian, S.-C. Zhang, and J.-F. Jia, Nat. Mater. **14**, 1020 (2015).

[21] J. Gou, L. Kong, H. Li, Q. Zhong, W. Li, P. Cheng, L. Chen, and K. Wu, Phys. Rev. Mater. **1**, 054004 (2017).

[22] C. Z. Xu, Y. H. Chan, P. Chen, X. Wang, D. Flötotto, J. A. Hlevyack, G. Bian, S. K. Mo, M. Y. Chou, and T. C. Chiang, Phys. Rev. B **97**, 035122 (2018).

[23] Y. Zang, T. Jiang, Y. Gong, Z. Guan, C. Liu, M. Liao, K. Zhu, Z. Li, L. Wang, W. Li, C. Song, D. Zhang, Y. Xu, K. He, X. Ma, S.-C. Zhang, and Q.-K. Xue, Adv. Funct. Mater. **28**, 1802723 (2018).

[24] J. Deng, B. Xia, X. Ma, H. Chen, H. Shan, X. Zhai, B. Li, A. Zhao, Y. Xu, W. Duan, S.-C. Zhang, B. Wang, and J. G. Hou, Nat. Mater. **17**, 1081 (2018).

[25] J. Yuhara, Y. Fujii, K. Nishino, N. Isobe, M. Nakatake, L. Xian, A. Rubio, and G. L. Lay, 2D Materials **5**, 025002 (2018).

[26] X. Zheng, J.-F. Zhang, B. Tong, and R.-R. Du, 2D Materials **7**, 011001 (2019).

[27] B. A. Bernevig, T. L. Hughes, and S.-C. Zhang, Science **314**, 1757 (2006).

[28] M. König, S. Wiedmann, C. Bruene, A. Roth, H. Buhmann, L. W. Molenkamp, X.-L. Qi, and S. C. Zhang, Science **318**, 766 (2007).

[29] B.-H. Chou, Z.-Q. Huang, C.-H. Hsu, F.-C. Chuang, Y.-T. Liu, H. Lin, and A. Bansil, New J. Phys. **16**, 115008 (2014).

[30] G. J. de Coster, P. A. Folkes, P. J. Taylor, and O. A. Vail, Phys. Rev. B **98**, 115153 (2018).

[31] J. Li and Y. Xu, arXiv:1909.09326 (2019).

[32] C.-X. Liu, H.-J. Zhang, B. Yan, X.-L. Qi, T. Frauenheim, X. Dai, Z. Fang, and S.-C. Zhang, Phys. Rev. B **81**, 041307(R) (2010).

[33] A. A. Baker, W. Braun, G. Gassler, S. Rembold, A. Fischer, and T. Hesjedal, Rev. Sci. Instrum. **86**, 043901 (2015).

[34] See Supplemental Material at http://link.aps.org/supplemental/10.1103/PhysRevB.100.245144 for additional information on sample characterization, ARPES light polarization dependence, and DFT calculations.

[35] E. Wimmer, H. Krakauer, M. Weinert, and A. J. Freeman, Phys. Rev. B **24**, 864 (1981).

[36] H. Krakauer, M. Posternak, and A. J. Freeman, Phys. Rev. B **19**, 1706 (1979).

[37] S. H. Vosko, L. Wilk, and M. Nusair, Can. J. Phys. **58**, 1200 (1980).

[38] C. Li, A. J. Freeman, H. J. F. Jansen, and C. L. Fu, Phys. Rev. B **42**, 5433 (1990).

[39] T. Osaka, H. Omi, K. Yamamoto, and A. Ohtake, Phys. Rev. B **50**, 7567 (1994).

[40] P. Fantini, S. Gardonio, P. Barbieri, U. del Pennino, C. Mariani, M. G. Betti, E. Magnano, M. Pivetta, and M. Sancrotti, Surf. Sci. **463**, 174 (2000).

[41] H. Zimmermann, R. C. Keller, P. Meisen, H. Richter, and M. Seelmann-Eggebert, J. Electron. Mater. **25**, 1293 (1996).

[42] D. M. Mahler, J.-B. Mayer, P. Leubner, L. Lunczer, D. Di Sante, G. Sangiovanni, R. Thomale, E. M. Hankiewicz, H. Buhmann, C. Gould, and L. W. Molenkamp, Phys. Rev. X **9**, 031034 (2019).

[43] J. Linder, T. Yokoyama, and A. Sudbø, Phys. Rev. B **80**, 205401 (2009).

[44] F. Zhang, C. L. Kane, and E. J. Mele, Phys. Rev. B **86**, 081303(R) (2012).